Inelastic processses from vibrationally excited states in slow $H^+ + H_2$ and $H + H_2^+$ collisions. II. Dissociation

P. S. Krstić[1] and R. K. Janev[2,3]
[1]*Physics Division, Oak Ridge National Laboratory, Oak Ridge, Tennessee 37831-637*
[2]*Macedonian Academy of Sciences and Arts, 1000 Skopje, Macedonia*
[3]*Forschungszentrum Juelich, Institute for Plasma Physics, D-52425 Juelich, Germany*
(Received 11 September 2002; published 26 February 2003)

We present a detailed quantum-mechanical study for dissociation of vibrationally excited molecular diatomic target, of $H_2(\nu_i)$ by proton impact and $H_2^+(\nu_i)$ by hydrogen-atom impact, in the range of center-of-mass collision energies from threshold to 9.5 eV. The dominant dissociation mechanisms in this three-atomic collision system are identified and their effectiveness analyzed for different collision geometries. The cross section calculations for direct and charge-transfer dissociation are performed by solving the Schrödinger equation for the nuclear and electronic motions on the two lowest diabatic electronic surfaces of H_3^+, and by using an expansion of nuclear wave function in a vibrational basis containing all discrete H_2 and H_2^+ states and a large number of pseudostates from each of the corresponding discretized continua. The energy and angular spectra of the fragments are also calculated and analyzed.

DOI: 10.1103/PhysRevA.67.022708 PACS number(s): 34.10.+x, 34.50.−s, 34.60.+z, 82.37.Np

I. INTRODUCTION

The dissociation processes in slow $H^+ + H_2$ and $H + H_2^+$ collisions play an important role in the energy and particle redistribution in all hydrogenic astrophysical and fusion divertor plasmas at temperatures above the relevant dissociation thresholds (about 4.54 eV for H_2 and 2.63 eV for H_2^+, in the ground vibrational states). The role of these processes is particularly pronounced when the hydrogen molecules, or molecular ions, are vibrationaly excited. The dissociation exibits a rapid increase of its cross section with increasing initial vibrational excitation and the corresponding decrease of their threshold energies. At plasma temperatures above 5–6 eV, the dissociation processes of vibrationaly excited H_2 and H_2^+ with protons and neutral hydrogen atoms, respectively, start to compete with the charge transfer processes, the latter being considered as an important mediating process in the volume recombination of fusion divertor plasmas [1].

The information on dissociation cross sections in these collision systems is very sparse, and only one set of classical, trajectory surface hoping (TSH) results [2] exists for the $H^+ + H_2$ system. Within the TSH method, the vibrational and rotational motions of the system are treated classically, while the electronic transitions are approximated by the Landau-Zener model along a classical trajectory of motion of the projectile. The results obtained by the TSH method need to be tested against the results of an *ab initio,* fully quantum-mechanical calculation. Furthermore, information on energy and angular distributions of dissociation fragments, important for the modeling of neutral particle energy and momentum transport in a low-temperature plasma, is completely absent in the literature. Dissociation cross section data for the $H + H_2^+$ collision at eV collision energies also are not available. All this provides a strong motivation for undertaking a comprehensive study of dissociative processes in these two collision systems.

In the present article we report on fully quantal dissociation cross sections as well as on energy and angular spectra of the fragments for the $H^+ + H_2(\nu_i)$ and $H + H_2^+(\nu_i)$ collisions from the ground and all excited vibrational states ν_i of H_2 and H_2^+, in the center-of-mass (c.m.) collision energy range from the dissociation threshold to 9.5 eV. We also identify and discuss in some detail the physical mechanisms responsible for the dissociation process, and their effectiveness at various collision geometries. We solve the Schrödinger equation for both electronic and nuclear motion, on the two lowest, strongly coupled adiabatic electronic energy surfaces of H_3^+, expanding the nuclear wave function in a vibrational basis consisting of all bound and a large number of discretized continuum states. To include possible processes of nuclear particle interchange, a large configuration space of reactants was spanned [3]. Thus, the vibrational coordinate ρ of the diatomic target, as well as the reactive coordinate R (between the projectile and c.m. of the target) were extended up to 40 a.u. Because the extent of the highest bound vibrational wave functions of H_2 and H_2^+ is somewhat above 10 a.u., the chosen space dimensions cover all reactive three-particle geometries. The charge transfer and vibrational excitation cross sections calculated in our previous work [4] fully confirm this statement. In the present work we use the sudden approximation for rotations, infinite order sudden approximation (IOSA) [5–8]. This approximation is applicable as long as the collision time is short compared to a typical rotation time, so that the rotation of a diatomic target may be considered frozen during a typical collision event. To account for the anisotropy of the energy surface, the calculation is repeated for various $(\vec{R},\vec{\rho})$ angles γ. The obtained cross sections are averaged over γ, in the interval 0°–180°. As discussed previously [4], this approximation works well in the eV region of collision energies, $E_{\text{c.m.}}$, and for molecular systems with a high degree of nuclear symmetry such as is H_3^+. Its accuracy is improved with the increase of ν_i -vibrational state manifold of rotational states, as well as with increase of $E_{\text{c.m.}}$. For the dis-

sociation processes considered here, with threshold of several eV from the lowest states, and for excited initial vibrational states, the use of IOSA does not constitute a serious limitation of the calculations. The two lowest adiabatic electronic potential surfaces, on which the dynamics of the system is considered, are constructed with the diatom-in-molecule (DIM) method [9,10] using the best available potential curves for the diatomic fragments ($1s\sigma_g$ and $2p\sigma_u$ of H_2^+, and the ground state $^1\Sigma_g^+$ of H_2 [11]), which were calculated *ab initio* for a large number [4] of diatomic internuclear distances to provide a smooth interpolation of the DIM surfaces, reducing the numerical errors to a minimum (more than 10^7 DIM geometries). The accurate potential curves of the fragments guarantee that the DIM potential energy surfaces (PES) tend asymptotically (in both R and ρ) to the exact values, which provides correct boundaries for the scattering problem. Since DIM is the most accurate in isotropic regions of the PES its application here is also supported by the high degree of nuclear symmetry in the system studied. More details on construction of the present DIM surfaces can be found in Ref. [4]. In order to asses the accuracy of the obtained DIM surfaces we compare them with adiabatic surfaces for the ground and the first excited states of H_3^+ obtained previously [12] by utilizing a 54-state $(11s,6p)$ Gaussian basis in the unrestricted-Hartree-Fock–(full)-configuration-interaction (UHF-CI) approach, using GAMESS [13]. As a measure of the accuracy of the DIM PES we define rms of the relative deviations of the DIM ($E_{\rm DIM}^{(i)}$) from the CI energies ($E_{\rm CI}^{(i)}$) at the ith PES, $\delta^{(i)}=(E_{\rm DIM}^{(i)}-E_{\rm CI}^{(i)})/E_{\rm CI}^{(i)}$. The r.m.s. $\overline{\delta}^{(i)}(R)$ is obtained by averaging of $\delta^{(i)}$ over ρ in the interval (0.5,10) a.u. for fixed value of R. Thus, for the ground H_3^+ PES, for $\gamma=90°$, we obtain $\overline{\delta}^{(1)}(R=1)=1.12\%$, $\overline{\delta}^{(1)}(3)=0.71\%$, $\overline{\delta}^{(1)}(5)=0.59\%$, $\overline{\delta}^{(1)}(7)=0.26\%$, and $\overline{\delta}^{(1)}(10)=0.17\%$. On the other hand, for the first excited PES of H_3^+ it follows $\overline{\delta}^{(2)}(R=1)=3.21\%$, $\overline{\delta}^{(2)}(3)=1.05\%$, $\overline{\delta}^{(2)}(5)=0.76\%$, $\overline{\delta}^{(2)}(7)=0.17\%$, and $\overline{\delta}^{(2)}(10)=0.17\%$. The accuracy of the DIM PES decreases toward smaller R, where anisotropy increases. For the same reasons the accuracy decreases for smaller angles γ.

The electronic matrix elements of nonadiabatic couplings (of $\partial/\partial R$ and $\partial/\partial\rho$), needed for transformation into the diabatic electronic basis are normally not available form quantum chemistry calculations. On the other hand, the DIM method enables an efficient calculation of the matrix elements, which is our main motivation for using this method, consistently for both PES and the matrix elements.

The technical detail of the method used in the calculations [14], as well as the associated numerical procedure are given elsewhere [4,7,14] and will not be repeated here. Therefore, in Sec. II we give only the basic system of coupled equations used for construction of adiabatic vibronic states and analyze the topology of electronic potential energy surfaces when the collision geometry (the angle γ) changes. In Sec. III we discuss the basic couplings between the vibronic adiabatic states in this system and the promotional series of these couplings leading to dissociation. In Sec. IV, the cross section for dissociation of both H_2 by proton and H_2^+ by hydrogen atom are presented for different vibrationally excited states of the target. The cross sections are compared with respect to the operating physical mechanisms for both diatomic targets. The energy and angular spectra of dissociation fragments are analyzed in Sec. V. Finally, in Sec. VI we give some concluding remarks.

The subject of the present article is thus the reactions

$$H^+ + H_2(v_i) \rightarrow H^+ + H + H, \tag{1}$$

$$H + H_2^+(v_i) \rightarrow H + H^+ + H, \tag{2}$$

$$H^+ + H_2(v_i) \rightarrow H + H^+ + H, \tag{3}$$

$$H + H_2^+(v_i) \rightarrow H^+ + H + H, \tag{4}$$

where $v_i=0-14$ in $H_2(v_i)$ and $v_i=0-18$ in $H_2^+(v_i)$. The reactions (1) and (2) are direct dissociation and (3) and (4) are dissociative charge transfer. Atomic units will be used in this work, unless otherwise explicitly stated.

II. COUPLED EQUATIONS FOR ADIABATIC VIBRONIC STATES

The complete formulation of the low-energy dynamics in the collision systems $H^+ + H_2(v_i)$ and $H + H_2^+(v_i)$ was given in our previous work [4]. Below we give only the results from that work relevant for our present calculations and discussions. Within the IOSA, and confining ourselves to the two lowest strongly coupled diabatic electronic states of H_3^+ system, the Schrödinger equation gives [15]

$$\left[-\frac{1}{2\mu}\left(\frac{\partial^2}{\partial R^2}+\frac{\partial^2}{\partial\rho^2}\right)+W_{11}+\frac{l(l+1)}{2\mu R^2}-E\right]\Psi_1(R,\rho;\gamma) + W_{12}\Psi_2(R,\rho;\gamma)=0, \tag{5}$$

$$\left[-\frac{1}{2\mu}\left(\frac{\partial^2}{\partial R^2}+\frac{\partial^2}{\partial\rho^2}\right)+W_{22}+\frac{l(l+1)}{2\mu R^2}-E\right]\Psi_2(R,\rho;\gamma) + W_{21}\Psi_1(R,\rho;\gamma)=0, \tag{6}$$

where E is the total energy of the system, l is the angular momentum of the projectile motion, W_{ij} are the coupling elements of diabatic Hamiltonian, and R and ρ are expressed in the mass-scaled coordinates of Delves [16] in terms of R and ρ coordinates defined in Sec. I (written here with primes for convenience)

$$R=aR', \quad \rho=a^{-1}\rho' \tag{7}$$

with

$$a=\left(\frac{\mu_{A,BC}}{\mu_{BC}}\right)^{1/4}. \tag{8}$$

$\mu_{A,BC}$ is the reduced mass of the $A+BC$ system, where A is a projectile and BC is the molecular target with reduced mass μ_{BC}. The reduced mass of the whole mass-scaled system is

$$\mu=\left(\frac{M_A M_B M_C}{M_A+M_B+M_C}\right)^{1/2} \tag{9}$$

and is independent of the nuclear configuration. The first of the considered two states represents the ground state of H_3^+ which for $R\to\infty$ has the dissociation limit $H^+ + H_2(^1\Sigma_g^+)$. The second of these two states is the first excited state of H_3^+ ion, which corresponds to the $H(1s)+H_2^+(1s\sigma_g)$ configuration. The second excited state of H_3^+ ion would be an anti-bonding state (of different, triplet symmetry than the first two states) and corresponds to the $H(1s)+H_2^+(2p\sigma_u)$ configuration.

In the adiabatic limit of the perturber (projectile) motion, the kinetic energy operator of the projectile relative motion (including its angular component) can be removed from Eqs. (5),(6), which yields an adiabatic eigenvalue problem for the coupled vibrational motion on the two diabatic electronic surfaces for each given diatomic orientation angle γ,

$$\left[-\frac{1}{2\mu}\frac{\partial^2}{\partial\rho^2}\mathbf{I}+\mathbf{W}(\rho,R)-\mathbf{E}(R)\right]\mathbf{\Phi}(\rho,R)=0, \tag{10}$$

where $\mathbf{W}$, $\mathbf{E}$, $\mathbf{\Phi}$, and $\mathbf{I}$ are the matrices

$$\mathbf{W}(\rho,R)=\begin{bmatrix} W_{22}(\rho,R) & W_{12}(\rho,R)\\ W_{21}(\rho,R) & W_{22}(\rho,R)\end{bmatrix},$$

$$\mathbf{E}(R;\gamma)=\begin{bmatrix} \varepsilon_1(R) & 0\\ 0 & \varepsilon_2(R)\end{bmatrix},$$

$$\mathbf{\Phi}(\rho,R)=\begin{bmatrix}\varphi_1(R,\rho)\\ \varphi_2(R,\rho)\end{bmatrix},\quad \mathbf{I}=\begin{bmatrix}1 & \\ & 1\end{bmatrix}, \tag{11}$$

defined for a fixed R. This eigenvalue problem was solved with finite quantization ''volume'' boundary conditions $\mathbf{\Phi}(\rho_{\max},R)=\mathbf{\Phi}(\rho=0,R)=0$, where $\rho_{\max}=40$ a.u. As a consequence, the relevant vibronic continuum is discretized, although with this choice of large $\rho_{\max}$ the density of the continuum states is very high even for several eV above the continuum edge. For each γ, the eigenvalue problem is solved for the lowest 900 vibronic eigenenergies $\mathbf{E}_i$ and eigenfunctions $\mathbf{\Phi}_i$, varying R as a parameter.

If the N eigenfunctions, $\mathbf{\Phi}_i$, $i=1,2,\ldots,N$ are used as an expansion basis for Ψ_j, $j=1,2$ to solve the coupled equations (5),(6), the only residual coupling would be the nonadiabatic coupling along the reactive coordinate, arising from the kinetic energy operator $\partial^2/\partial R^2$. This coupling takes the form

$$\left\langle \mathbf{\Phi}_i\left|\frac{\partial^2}{\partial R^2}\right|\mathbf{\Phi}_j\right\rangle,\quad U_{ij}(R)\frac{\partial}{\partial R}, \tag{12}$$

where

$$U_{ij}(R)=\left\langle \mathbf{\Phi}_i\left|\frac{\partial}{\partial R}\right|\mathbf{\Phi}_j\right\rangle=\int d\rho\,\mathbf{\Phi}_i^T(\rho;R)\frac{\partial}{\partial R}\mathbf{\Phi}_j(\rho;R), \tag{13}$$

where $i,j=1,2,\ldots N$, ''T'' means matrix transpose. After introducing such an expansion in Eqs. (5),(6), the resulting system of coupled equations for the adiabatic vibronic states defines the entire slow collision dynamics of the system on the two lowest, strongly coupled diabatic electronic states of the H_3^+ for a fixed collision geometry (angle γ).

Insight in the collision dynamics of a heavy-particle collision system can be gained from an analysis of the behavior of its adiabatic potential energy curves (surfaces). We shall postpone such an analysis of adiabatic vibronic energies to the next section, where the dissociation mechanisms will be discussed. Here we note a general feature of the H_3^+ system that dominates collision dynamics on the two lowest potential energy surfaces, the formation of an avoided intersection line (seam) between these two potential energy surfaces in the adiabatic representation of electronic states. For $\gamma=90°$, the seam appears at $\rho=\rho_s\simeq 2.5$ and $R\gtrsim 4.5$, and along it the matrix elements of $\partial/\partial\rho$ between the adiabatic electronic states are almost delta functions of the vibrational coordinate. This ''numerically violent'' behavior of matrix elements of $\partial/\partial\rho$ in the adiabatic electronic basis is the reason for using the diabatic representation [17] of electronic states on which the vibrational dynamics is considered. For other values of γ the seam position changes slightly, but it remains narrow. This is illustrated on Fig. 1 for the collision geometry defined by $\gamma=53.13°$. Figure 1(a) shows the 3D plots of the adiabatic electronic energies of the two states considered, Fig. 1(b) shows the equienergy contours of the ground electronic state, while Figs. 1(c) and 1(d) show the 3D plots of matrix elements of $\partial/\partial R$ and $\partial/\partial\rho$ between the two adiabatic states. Variation in the shape of the adiabatic energy surfaces and the coupling matrix elements as the collision geometry changes is quite significant; this indicates that the collision dynamics is strongly dependent on the orientation of molecular axis with respect to the vector of reactive coordinate $\vec{R}$. One can see from Fig. 1(b) that a new potential minimum (not visible for $\gamma=90°$ starts to be formed on the adiabatic energy surface of the ground electronic state on the other side of the seam, and in the limit of a strict colinear geometry ($\gamma=0$), the potential well of the H_3^+ ion becomes a symmetric double-potential well. The axes of two wells make approximately angle of $\theta_s=60°$, as follows for the H_3^+ system, in the mass-scaled coordinates [18]. Namely, the angle between reactant and product potential configurations depends on the mass of the particles that chemically interact. In addition to these two wells, there is another potential well configuration at small γ's, separated by a large repulsive (for low collision energies almost inpenetrable) barrier, formed by the projectile-target nuclear repulsion.

The structure of matrix elements of $\partial/\partial R$ and $\partial/\partial\rho$ becomes increasingly more complex and more peaked with de-

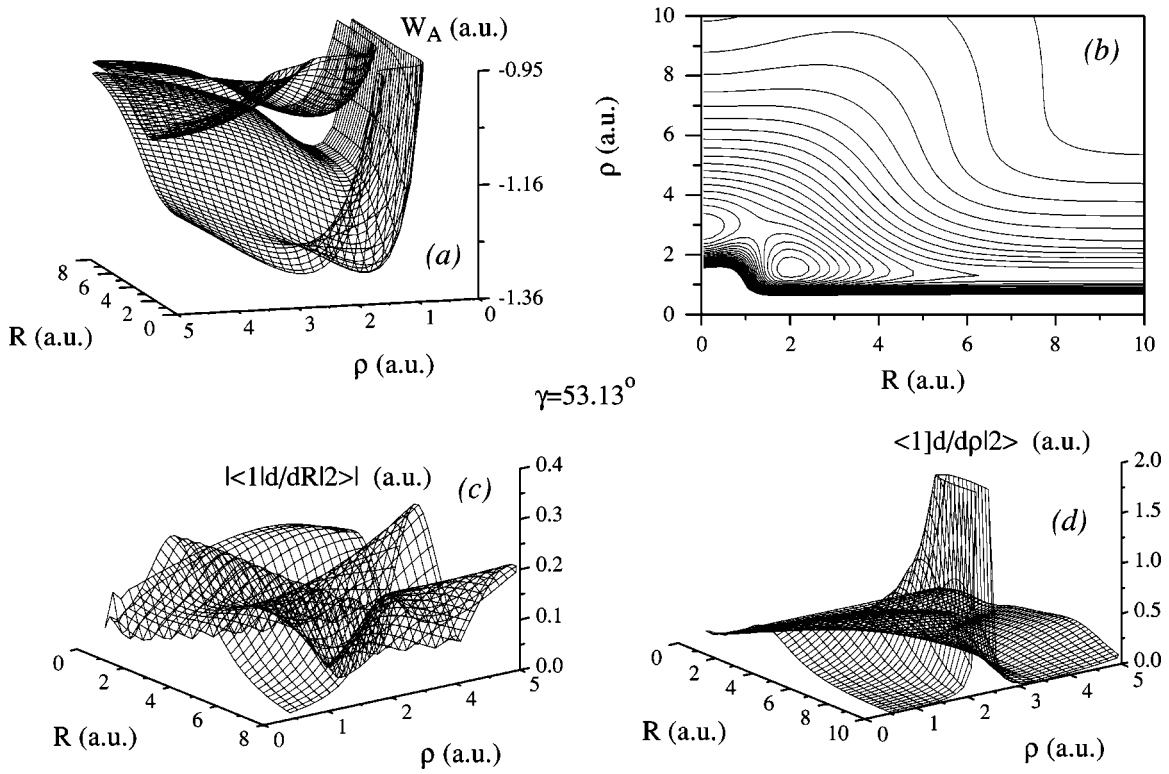

FIG. 1. Adiabatic electronic energy surfaces and nonadiabatic couplings between the electronic states, for $\gamma=53.13°$. (a) Two lowest surfaces of H_3^+. (b) Contour plot of the lowest surface. (c) Nonadiabatic matrix element of $\partial/\partial R$ between the two electronic states. (d) Nonadiabatic matrix element of $\partial/\partial\rho$ between the two electronic states.

creasing γ. Thus, for $\gamma=90°$, $\langle 1|\partial/\partial R|2\rangle$ has a relatively smooth character in the (R,ρ) plane, whereas for $\gamma=8.11°$ its structure becomes much more complex (including formation of series), and is very strongly peaked (not shown in the figures). The matrix element $\langle 1|\partial/\partial\rho|2\rangle$ for $\gamma=90°$ is strongly peaked only along the seam, whereas for $\gamma=8.11°$ its behavior shows similar characteristics as that of $\langle 1|\partial/\partial R|2\rangle$. At this place, however, we shall refrain from a detailed analysis of the structure of matrix elements of $\partial/\partial R$ and $\partial/\partial\rho$ between adiabatic electronic states, and their relation to specific aspects of the collision dynamics. For the purposes of the present work, we shall rather confine ourselves to a similar analysis of matrix elements of $\partial/\partial R$ between the vibronic adiabatic states constructed on the diabatic electronic potentials, as discussed earlier.

III. DISSOCIATION MECHANISMS

The transitions between adiabatic vibronic states are caused by a number of nonadiabatic couplings of different types. All of these types of couplings have their origin in the operator $\partial/\partial R$ acting on the adiabatic vibronic functions, but they are all characterized by additional features arising from the local behavior of the adiabatic vibronic energies and nonadiabatic interactions. These features can be especially well elucidated if one considers the topology of adiabatic vibronic energies in the complex plane of reactive coordinate R. In order to illustrate couplings, we show in Fig. 2(a) the energies of adiabatic vibronic states for the $\gamma=90°$ geometry as function of reactive coordinate R, which in the dissociation limit correspond to the states $H^+ + H_2(v=2,3,4,8)$ and $H + H_2^+(v'=0',1',5',6')$ (the latter are shown by dashed lines). In Fig. 2(b) we show the couplings $U_{i,j}(R)$ between these states. First we note that the energies of states $v=2,3$

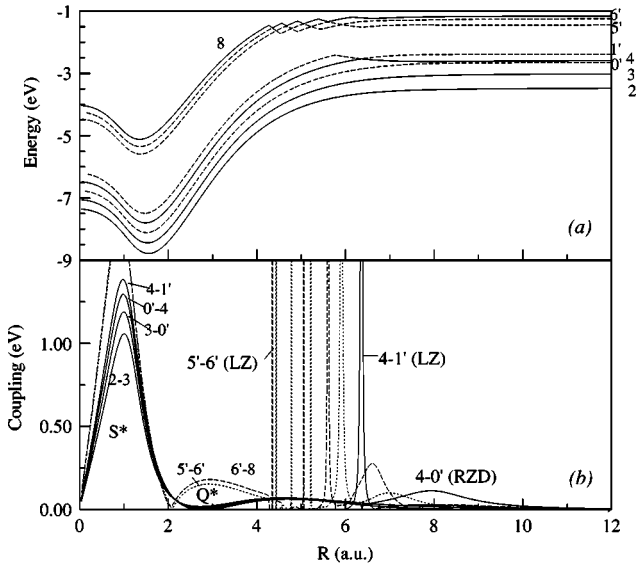

FIG. 2. Characteristic vibronic adiabatic energy terms and type of nonadiabatic couplings between them. LZ: Landau-Zener, RZD: Rozen-Zener-Demkov, Q^* and S^* are the types of hidden crossings (example of $\gamma=90°$).

do not "intersect" the energies of v' states; the energy of state $v=4$ closely approaches that of state $v'=0'$ for $R \approx 7$ and for the larger values of R the two curves become practically parallel and nearly resonant. The energy of state $v=4$ also has a narrow avoided crossing with the energy of state $v'=1'$ at $R \simeq 6.4$. At the position of avoided energy crossing of states $|4\rangle$ and $|1'\rangle$ the coupling matrix element between these two states shows a narrow and strongly pronounced peak [see Fig. 2(b)], a situation typical for the Landau-Zener (LZ) type of coupling between two adiabatic states. The behavior of adiabatic energy curves of the states $|4\rangle$ and $|0'\rangle$ in the region around $R \sim 8$ and beyond, and the peaking of radial matrix elements between these two states in this region [see Fig. 2(b)], indicate that the states are coupled by a Rosen-Zener-Demkov (RZD) nonadiabatic coupling mechanism. A general characteristic of LZ and Demkov couplings in an ion-atom collision is that they couple adiabatic states which are centered asymptotically on different centers. Here, these mechanisms couple vibronic states for different nuclear configurations, $H^+ + H_2$ and $H + H_2^+$, causing electron transfer from H_2 onto H (or vice versa).

From Fig. 2(b) we see that the radial matrix elements, Eq. (13), between successive states (e.g., $|2\rangle$ and $|3\rangle$, $|3\rangle$ and $|0'\rangle$, $|0'\rangle$ and $|4\rangle$, and $|4\rangle$ and $|1'\rangle$), although couple states which are asymptotically centered at either one or both of the H_2 or H_2^+, have relatively broad maxima in the region around $R \sim 1$. It can be noticed from this figure that the maximum of matrix element 4-1′ at $R \sim 1$ is slightly shifted towards the smaller values of R with respect to the matrix element 2-3. Pronounced couplings appear also between all successive states, starting with $v=4$, at $R \sim 3$; only those for 5′-6′ and 6′-8 are shown in Fig. 2(b) (as the strongest among them). In order to investigate the nature of these couplings, we have calculated the energies of these selected states in the complex plane of R and found that the corresponding energy surfaces are pairwise connected by branching points ("hidden crossings") in the regions $\mathrm{Re}\{R\} \sim 1$ and $\mathrm{Re}\{R\} \sim 3$. Based on the positions of the real parts of the hidden crossings R_c for these pairs of states (as well as others for higher states), we concluded that the hidden crossings in the region $\mathrm{Re}\{R_c\} \sim 1$ are similar to the S-type hidden crossings in the two-Coulomb center electron problem [19] (they are concentrated in a small region δR in the complex plane). The hidden crossings in the region around $\mathrm{Re}\{R_c\} \sim 3$ show similarities with the Q-type hidden crossings in the two-Coulomb center problem. Consequently, we denote the couplings in the regions $R_S \sim 1$ and $R_Q \sim 3$ as S^*-type and Q^*-type hidden crossing couplings, respectively. The appearance of an S^*-type branch point is associated with the strong Coulomb repulsion of the projectile and target nuclei for small values of reactive coordinate. This interpretation underscores the analogy with the origin of the S-type branch points in the case of two-Coulomb center single-electron case, where a negatively charged (antiproton) projectile creates a repulsive Coulomb barrier for the electron [20]. In the case of a positively charged projectile, the centrifugal Coulomb barrier plays the same role. The appearance of the Q^*-branch points is associated with the change of the character for adiabatic vibronic functions, i.e., from predominantly three atomic on the left side of $\mathrm{Re}\{R_Q\}$ to predominantly diatomic on its right side. As seen from the form of Q^*-type couplings in Fig. 2(b), the extent of the region of R within which this change of the wave function character takes place is quite sizeable. We note that a LZ avoided crossing for two adiabatic states corresponds to a real hidden crossing in the complex R plane, an image of which on the real R axis is the avoided crossing. Similarly, the RZD coupling of the states $|4\rangle$ and $|0'\rangle$ in the region about $R \simeq 8$ corresponds to a series of hidden crossings $R_{c,j}$ between the adiabatic energy surfaces of these states in the complex R plane; each has the same real part and equidistantly displaced imaginary parts [19]. The width and the peak values of the radial coupling element arround $\mathrm{Re}\{R_c\}$ are related to the value of $\mathrm{Im}\{R_c\}$ of corresponding hidden crossing point R_c in the complex plane (i.e., the closer R_c is to the real axis, the higher ($\sim \mathrm{Im}\{R_c\}$) and narrower ($\sim 1/\mathrm{Im}\{R_c\}$) the peak). Therefore, the hidden crossings that lie close to the real axis are associated with the strongest nonadiabatic couplings. This is usually the case with the hidden crossings that connect two successive adiabatic energy surfaces. Thus, the topological features of the adiabatic energy surface in the complex R plane are directly related to the nonadiabatic couplings in the system and, consequently, to its dynamics.

From the structure of adiabatic vibronic energy spectrum of H_3^+ ion (which at $R \to \infty$, in our case, goes over into the diatomic vibrational spectrum either of H_2 or H_2^+), and the fact that the radial coupling is the strongest for two successive adiabatic states (see the discussion above), it follows that the S^*-, Q^*-, and LZ-type branch points form series along the entire part of discrete spectrum that lies above the initial vibronic state. If the continuum states are also discretized, as in the approach followed in the present paper, these series of hidden crossings extend also in the continuum. Therefore, such series of branch points (or series of strong radial couplings between the successive adiabatic vibronic states) promote the system into its dissociation continuum in the course of the collision. The RZD couplings, that require near-resonant energy conditions for the coupled states in order to be effective (conditions that cannot be met for any two successive states in the vibronic spectrum), do not form promotive series for dissociation. They, however, do participate in the overall vibrational dynamics.

The position of promotive dissociation series on the coordinate R, as well as their effectiveness, strongly depend on the collision geometry. In Fig. 3(a) we show the energies of the 100 lowest vibronic adiabatic states $\mathcal{E}(R;\gamma=90°)$ [Eq. (10)] for orthogonal geometry of the projectile and diatomic target. The solid lines represent three-atomic adiabatic states which asymptotically ($R \to \infty$) become the vibrational states of H_2, while dashed lines represent the energies of states that asymptotically go to the H_2^+ [shifted by the binding energy of the projectile $H(1s)$]. We note that the continuum edge, defined by the first vibronic state which has asymptotically a positive energy (the thick solid line), is strongly deformed in the course of collision due to the deeper potential well of the H_3^+ ion (about -9.5 eV in this geometry) with respect to

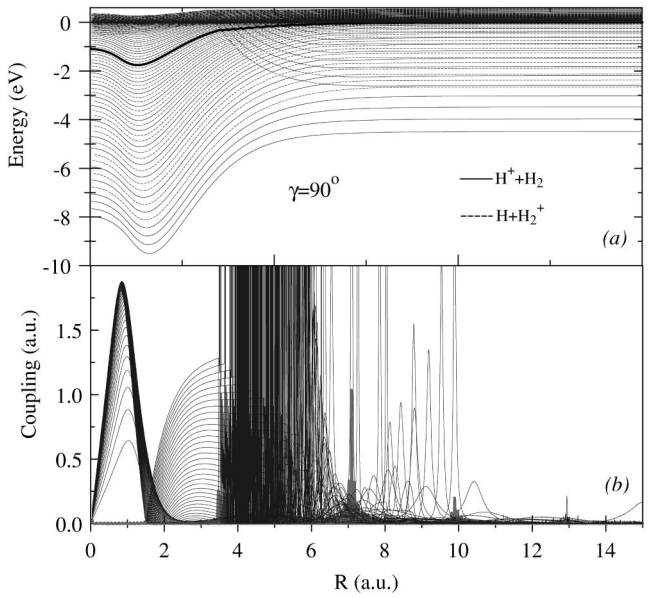

FIG. 3. (a) Energy term diagram of adiabatic vibronic states when $\gamma=90°$ and (b) nonadiabatic coupling matrix elements $\langle i|\partial/\partial R|i+1\rangle$ between successive states.

potential wells of H_2 and H_2^+. The deeper potential well of three-atomic collision complex can accommodate a larger number of bound states than the sum of bound states of its diatomic asymptotic fragments. The number of such collisionally induced vibrational bound states (CIVBS) progressively increases when the projectile approaches the distance at which the potential energy of H_3^+ attains its minimum, and starts to decrease for still smaller R (due to the increased nuclear repulsion). The CIVBS have an analogy in the so-called light-induced bound states (LIS) when atom is subjected to a laser field of an increasing intensity [21]. The CIVBS can obviously affect the overall vibrational dynamics of three-atomic systems and, in particular, the dissociative and associative processes in such systems, as discussed below.

The nonadiabatic matrix elements $|U_{ij}(R)|$ for $\gamma=90°$ and for all adjacent vibronic states ($j=i+1$, $j\leqslant 50$) are shown in Fig. 3(b). Since LZ couplings between continuum states gradually shift toward lower R, inclusion a larger number of $|U_{ij}(R)|$ in Fig. 3(b) would screen the main features of the nonadiabatic matrix elements between bound vibronic states. The localization of the promotive dissociation series of couplings is now visible to the full extent. The coupling matrix elements associated with the S^* series are concentrated in the region around $R\sim 1$, including those coupling CIVBS and higher. The good localization of this series of couplings, and the gradual shift of their maxima towards smaller R, are indications that this series constitutes a strong dissociation channel during the incoming stage of the collision. As the vibrational state increases the peak values of the coupling matrix elements tend to saturate, but their halfwidths gradually decrease. Thus, for the higher states we get $\mathrm{Im}\{R_c\}\sim 0.5$, typically, while for the lower states $\mathrm{Im}\{R_c\}\sim 2$. This indicates that the higher vibrational states are dissociated more easily than the lower ones. The S^* promotive

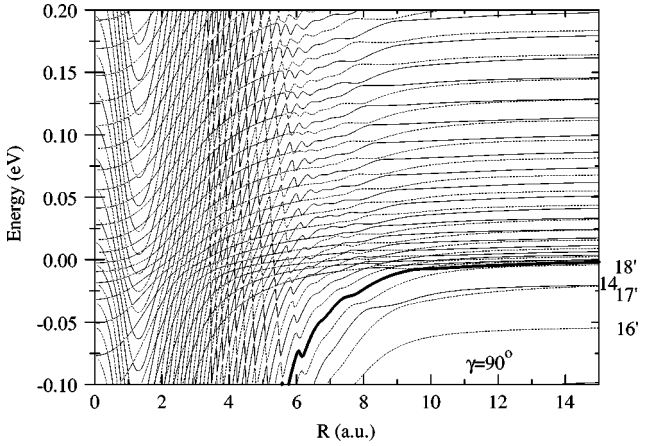

FIG. 4. The diagram in Fig. 3(a), zoomed around the continuum edge.

series brings the system deeply in the continuum where it also remains after the collision. A smaller part of the probability flux brought into the CIVBS region can be captured back to the bound states during the receding stage of the collision along the same S^* series, but then it becomes subject of promotion to the continuum by the Q^* series of nonadiabatic couplings at $R\sim 3$. The Q^* series of couplings, however, is a relatively weak dissociation channel during the receding stage of the collision for two reasons. First, the halfwidths of coupling matrix elements associated with this series are quite large; this indicates a weak coupling of the states. Second, the higher terms of this series (for all states that asymptotically tend to the $v\geqslant 4$ and $v'\geqslant 0$) ''overlap'' a series of much stronger Landau-Zener transitions [see Fig. 3(b)] that divert the probability flux from the Q^* promotive path into the spectrum of discrete states. Both the S^* and Q^* series appear in the regions of R where there is an inflection in the adiabatic energy curves [see Fig. 3(a)]. Finally, for the collision systems $H^+ + H_2(v\geqslant 4)$ and $H + H_2^+(v'\geqslant 0)$ each of the initial states enters a series of successive LZ couplings during the incoming stage of the collision, that promote the system ''diabatically'' into the dissociation continuum following the position of the seam [see Figs. 3(a) and 3(b)]. Because the LZ series enter the continuum edge at relatively large distances R_d, the wave packet has enough time to expand in the continuum before it passes the points R_d again on the receding stage of the collision. The LZ diabatic promotion extends deeply into the continuum (Fig. 4) leading to higher energies of dissociated fragments. Similarly, RZD couplings also extend into the continuum, as seen in Fig. 4. Because both LZ and RZD matrix elements couple the target and corresponding charge-transfer continuum states (as they do in the discrete spectrum), they tend to equilibrate the direct and charge transfer channels of the dissociation process.

We note that the state $v=4$ is also promoted to the continuum by the lowest LZ series after its transition to the $v'=0$ by the RZD coupling at $R\simeq 8$. However, the states that asymptotically correspond to the $H_2(v=0-3)$ can be promoted to the continuum only by the S^* series at $R\sim 1$. The isolated couplings in Fig. 3(b) at R larger than ~ 6 have

relatively large halfwidth and are related to the RZD nonadiabatic coupling.

Potential energies of the two lowest electronic states of the system change with the change of collision geometry, therefore the strength and position of nonadiabatic couplings (as well as of their series) also change. Thus, energy curves for $\gamma=54.13°$ are deformed in the region below $R\sim1$ with respect to their behavior for $\gamma=90°$. Their decrease with decreasing of R is a consequence of the formation of a second potential well, as seen from Figs. 1(a),1(b). The deflection of potential curves near $R\sim0.25$–0.5 indicates a change of the character of adiabatic vibronic wave functions that now have to describe the motion of the system in the presence of the forming second potential well. The change is reflected in significant couplings between the states and the appearance of a Q^* series near $R\simeq0.28$. This series is fairly well localized because its extension is restricted by the vicinity of the potential barriers at $R\sim1$. The S^* series at $R\sim1$ is now more pronounced than in the $\gamma=90^{\circ}$ geometry (matrix elements are more peaked, and their peak values larger), and it extends deeper in the continuum. The Q^*-promotive series in the region $R\sim2.5$–3.5 is now weaker than in the case of $\gamma=90°$ geometry (the peaks of corresponding matrix elements are smaller and their widths larger). It should be noted that already for $\gamma=54.13°$ the promotive LZ series start to bend in the region of CIVBS spectrum and the lowest seven return back below the dissociative continuum edge (the thick solid line) before the system reaches the nuclear repulsive barrier near $R\sim1$. This behavior indicates that the diabatically promoted states in the continuum can be ''recaptured'' due to their interactions with the CIVBS. The ''recapture''effect, however, does not reduce the effectiveness of LZ promotive dissociation channels significantly. It is appearant a strong LZ mixing of the CIVBS and other continuum states that asymptotically correspond to the $(H+H)$ and $(H+H^+)$ continua. The positions of corresponding matrix elements overlap with the regions where the S^* and Q^* series are located.

With the further decrease of angle γ, the effects of formation of the second potential well in the three-atomic system become even more visible. Thus, the number of CIVBS significantly increases for the geometry $\gamma=25.84°$, and a potential barrier forms. The barrier even extends below the asymptotic continuum edge. The repulsive barrier around $R\sim1$ for $\gamma=54.13°$ is now shifted to larger values of R (~1.8–2.2), it becomes much broader and even disappears for the lowest states. Particle rearrangement (atom exchange) effects become pronounced in this region of R at the considered collision geometry. The S^* type of radial couplings along this barrier are now transformed into LZ type couplings, and the earlier promotive S^* series is replaced by a multitude of promotive LZ series. The Q^* series at $R\sim0.25$–0.3 for $\gamma=54.13°$ is now shifted to larger $R(\sim0.5$–$0.8)$, and, unrestricted by the strong Coulomb repulsion barrier, its coupling matrix elements extend over a broader range of R. The earlier Q^* series at $R\sim3$–4 is now limited to its several lowest coupling terms, while the couplings between the higher states are transformed into LZ-type couplings.

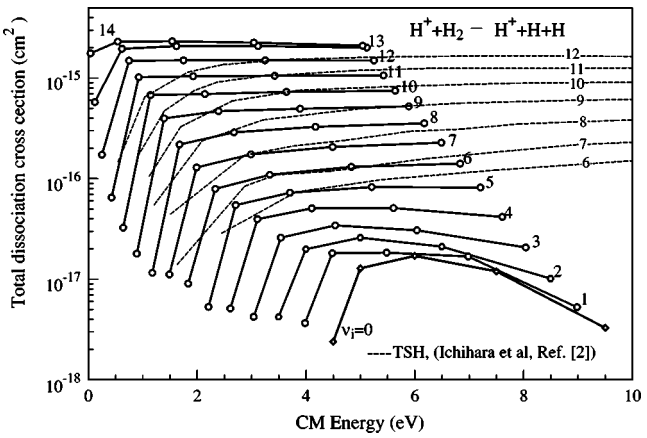

FIG. 5. Total dissociation cross section as function of the collisional c.m. energy, for the $H^+ + H_2$ (ν_i) system.

Finally, when the collision geometry is nearly collinear $(\gamma=8.11°)$ the formation of the second potential well in the system is nearly accomplished. The number of CIVBS for this collision geometry becomes very large and their energy structure represents a smooth extension of the energy structure of the states below the asymptotic continuum edge. Near the colinear arrangement, the symmetry properties (identity of the nuclei) of the system begin to manifest themselves, giving rise to symmetry splitting of adiabatic energies on both sides of the seam (particle exchange effect). States in the range $R\sim7$–11 show a broad and shallow energy minimum and are all diabatically promoted to the asymptotic continuum edge at distances of R smaller than $\simeq15$ as R increases. Dominant couplings between the adiabatic states in this collision geometry are the LZ couplings. The Q^* series of relatively weak couplings in the small-R region remain at this collision geometry (the maxima of Q^* couplings are now shifted to $R\sim1$), and a new similar, still weaker series emerges at $R\sim8$–10.

Analysis of the nonadiabatic couplings and the promotion mechanisms for dissociation processes in the H_3^+ collision system, and their role when the collision geometry changes, indicates that, in general (i.e., excluding the states with the asymptotics $v=0-3$), the Landau-Zener promotion series are the main dissociation mechanism in this collision system. As γ decreases, the number of CBVBS increases, and the LZ coupling series promote the system more and more deeply in the continuum. Consequently, the dissociation cross section increases with decreasing γ.

IV. CROSS SECTIONS FOR DISSOCIATION

The details of calculations using the coupled channel method are discussed in Ref. [4], and will not be repeated here. The total cross section $\sigma_{\rm tot}(\nu_i, E_{\rm c.m.})$ for dissociation from an initial vibrational state ν_i is calculated by summing the cross sections for transitions from an initial bound state ν_i to those vibrational states in the working basis which have positive energy. These could be discretized continuum states of either H_2 or H_2^+. Figure 5 shows $\sigma_{\rm tot}$ for dissociation of $H_2(\nu_i)$ in collision with H^+, while Fig. 6 presents $\sigma_{\rm tot}$ for

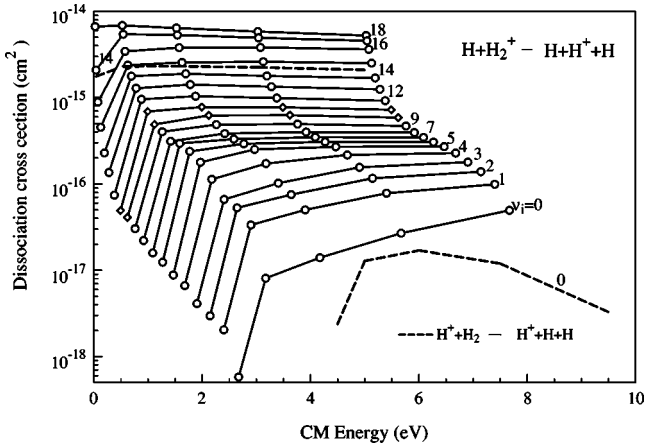

FIG. 6. Total dissociation cross section as function of the collisional c.m. energy, for the $H+H_2^+(\nu_i)$ system.

dissociation of $H_2^+(\nu_i)$ in collision with H(1s). Both H_2 and H_2^+ are initially in their respective ground electronic states, and ν_i spans all bound vibrational states ($\nu_i=0-14$ for H_2 and $0-18$ for H_2^+). The only reference for comparison is TSH calculation of Ichihara *et al.* [2] for the $H^+ + H_2$ collision system, which agrees well with our results (Fig. 5) in the region of higher collision energies and for the higher ν_i, as could be expected from the classical character of the TSH calculation. The peak values of the cross sections are almost uniformly distributed with ν_i over a span of two orders of magnitude. The dissociation cross section from lower $\nu_i's$ peaks in the range 6–4 eV, and their decrease can be associated with the increase of the competing CT process with increasing the energy. The shallow character of the potential well which supports the vibrational bound states of H_2^+ gives rise to larger (by a factor of 2–3 in average) total dissociation cross sections for $H+H_2^+(\nu_i)$ (Fig. 6). For comparison, the $\sigma_{tot}(\nu_i=0)$ for the $H^+ + H_2$ system is also shown in Fig. 6. Unlike CT in $H^+ + H_2(\nu_i) \rightarrow H+H_2^+$, the charge transfer $H+H_2^+(\nu_i) \rightarrow H^+ + H_2$ has exoergic components for all ν_i and, as a consequence, it is decreasing at higher energies [4]. Thus, the total dissociation cross sections in Fig. 6 do not reach their maxima in the considered energy range. The total cross sections in both Figs. 5 and 6, show a characteristic steep exponential decrease in the narrow range of energies above the threshold for dissociation from any initial vibrational state ν_i, followed by a much slower increase until the cross section maximum is reached.

The eigenstates of Eq. (10), as $R \rightarrow \infty$ separate to two disjunct, uncoupled sets that correspond to the vibrational states of two different Hamiltonians H_2 and H_2^+. The same is true for the quasidiscrete states of positive energy, that belong to the separate dissociative continua, those of H_2 and H_2^+. As discussed in the previous section, these states are strongly coupled mutually, thus enabling charge transfer and ''excitation'' in the continuum [also present in laser-atom ionization, and known as above threshold ionization (ATI)]. The coupling of the dissociative states of H_2 and H_2^+ can also be realized in indirect way, by CT followed by dissociation. All the processes are accompanied by the reverse pro-

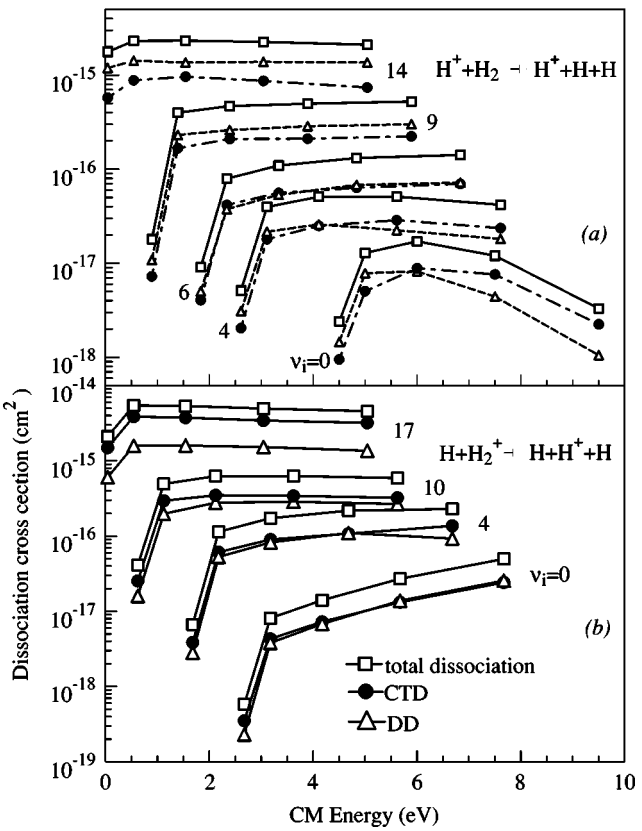

FIG. 7. Comparison of the dissociation components, direct and CT dissociation cross sections for different initial vibrational states ν_i of the target for (a) $H^+ + H_2(\nu_i)$ and (b) $H+H_2^+(\nu_i)$ collisions.

cesses in either half of the collision. By ''direct'' dissociation (DD) we consider the process(es) that lead to the dissociating fragments in the dissociation states of their parent, i.e., of the diatomic molecule that supported the initial vibrational state. Similarly, charge transfer dissociation (CTD) is process that leads to dissociating fragments of ''charge-transfer'' produced molecule (rather than of parent one). An example of the DD process is dissociation if $H_2(\nu_i)$ into H+H by proton impact. An example of CTD process would be the dissociation of $H_2(\nu_i)$ into $H+H^+$ by proton impact. Obviously, in this latter case the charged projectile will exit the scattering zone as a neutral H. These conclusions are also directly supported by the diagrams in Fig. 7, where DD and CTD cross sections are shown in the same graphs for various ν_i, for $H^+ + H_2$ in Fig. 7(a) and $H+H_2^+$ in Fig. 7(b). It is obvious that the DD is a stronger process than CTD for $\nu_i=14$ in Fig. 7(a), but the difference diminishes toward lower ν_i. At $\nu_i=6$ the contributions of DD and CTD to the total dissociation cross section are almost equal, and for even lower ν_i the DCT starts to be more a important process at the higher end of considered energy range. For the $H+H_2^+$ dissociation, the conclusions are somewhat opposite: for the higher ν_i, CTD dominates the total dissociation by more than a factor 2; this dominance diminishes toward lower ν_i, and for $\nu_i \leqslant 4$ the contributions of DD and CTD processes to the total dissociation cross section become practically equal. This consideration supports the assertion of the preceding section that DD

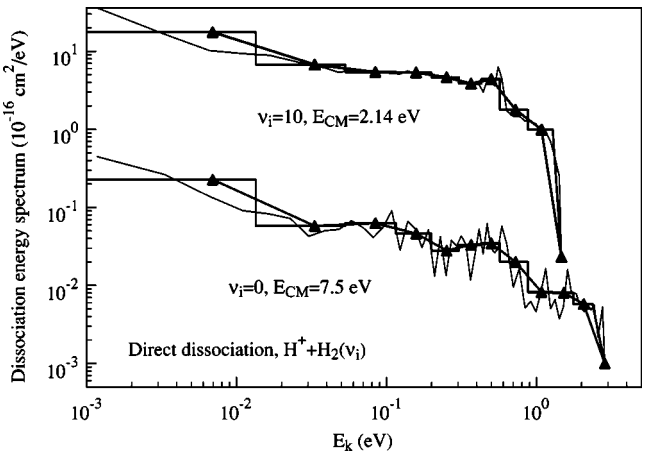

FIG. 8. Procedure for calculation of the dissociation energy spectra of the fragments (see text).

and CTD are almost equilibrated by the strong mixing in the continuum. The DD process is slightly more intensive from the higher excited states of H_2, while CTD is slightly more intensive from the lower lying states.

V. SPECTRA OF DISSOCIATION FRAGMENTS

We define the dissociation energy spectra as a cross section per unit (c.m.) energy interval of dissociating fragments. The choice of the energy interval(s) used for the calculation of the spectra may influence the shape of the spectra. To explain this, we show in Fig. 8 the energy density of the cross sections for dissociation of H_2 of the $H^+ + H_2(\nu_i)$ system (thin lines) from $\nu_i = 0$ and $\nu_i = 10$, respectively, as functions of energy of the fragments, for various projectile c.m. energies. The thin lines in this figure are energy spectra obtained as energy density of the cross sections, calculated from the subsequent points, i.e.,

$$\frac{\sigma}{\Delta E_k}(\overline{E}_{k,n}) = \frac{\sigma_{n+1} + \sigma_n}{E_{k,n+1} - E_{k,n}}, \tag{14}$$

where $\overline{E}_{k,n} = (E_{k,n+1} + E_{k,n})/2$. Due to the inhomogenity of continuum states (their density is large close to continuum edge and decreases with the energy of fragments) this picture changes substantially when we average over the oscillatory features of these spectra, by averaging the cross sections in the larger energy intervals, i.e.,

$$\left(\frac{\sigma}{\Delta E_k}\right)_{\text{av}} = \frac{\sum \sigma_n}{E_{k,n+m} - E_{k,n}}. \tag{15}$$

The examples of this procedure are presented with histograms in Fig. 8, for $m = 5$. Finally, by connecting midpoints of the histograms, the energy spectra shown in this section are obtained. m was chosen as the smallest integer that removes the oscillatory features of the spectra. The value of m chosen in that way also stabilizes the shape of spectra against further increase of the energy interval, although the spectra become gradually flatter.

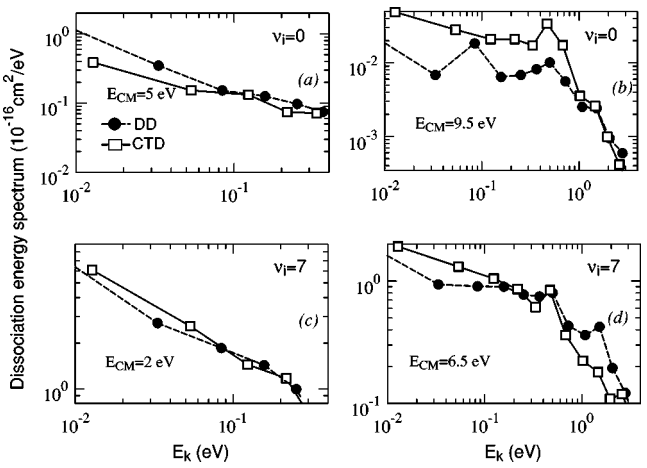

FIG. 9. Comparison of the energy spectra for direct and CT dissociation for $H^+ + H_2(\nu_i)$, at various collision energies and ν_i.

In Fig. 9, we present the energy spectra for DD and CTD of $H_2(\nu_i)$ in collision with proton for various c.m. energies of the projectile and for a number of representative values of ν_i. An obvious feature of these spectra is a pronounced cusp at the continuum edge for lower energies of the projectile. This feature is present for all initial states of the target molecule. The comparison of the total dissociation energy spectra for various ν_i and various c.m. collision energies, is expressed in Fig. 10 as values E_{ref} above the dissociation threshold $W(\nu_i)$ [i.e., $E_{\text{c.m.}}^{(\nu_i)} = W(\nu_i) + E_{\text{ref}}$]. The spectra extend close to E_{ref}, slowly decreasing with the fragment energy E_k, and then abruptly disappear, as required by the energy conservation. Figures 11 and 12 present dissociation energy spectra of $H_2^+(\nu_i)$ in collisions with H, and show similar features as the cases presented in Figs. 9 and 10.

We have also studied the distribution of dissociated fragments with respect to the angle γ. In Fig. 13 we show the angular distributions of dissociation fragments from the $H^+ + H_2$ dissociation (sum of DD and CTD channels) for the initial vibrational states $v = 0$ and 11 and a selected number of c.m. collision energies. The numbers on the concentric

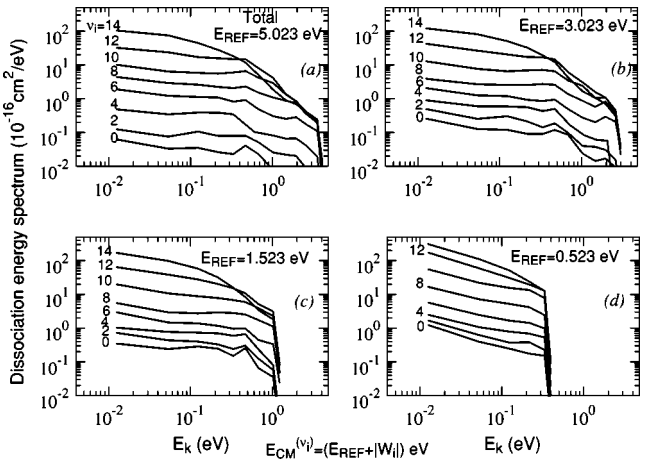

FIG. 10. Total dissociation energy spectra for the $H^+ + H_2(\nu_i)$ system, for all ν_i at representative c.m. collision energies.

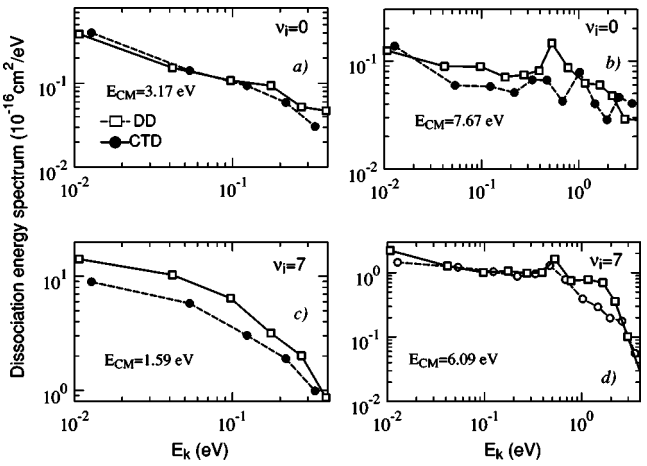

FIG. 11. The same as Fig. 9, for $H+H_2^+(v_i)$ collisions.

circles indicate the values of dissociation cross section (in units of cm^2). For the $v=0$ case, a cosine-type distribution is apparent for the higher energies (7.5 and 9.5 eV), while with decreasing the collision energy the distributions become increasingly more isotropic. In the case of $v=11$, however, the situation is reversed. We conveniently represent the angular spectra of dissociation products in the form

$$S_E(\gamma)=F(E)\{\cos^{\alpha}(\gamma)+b_E(v)\sin(\gamma)\}, \tag{16}$$

where α and $b_E(v)$ can be obtained by fitting the cross section data to the above expression. It has been found that the parameter α does not depend on the energy and, to a high accuracy, has the form

$$\alpha(v)=10.5(1+0.069v^{1.86})^{-1}. \tag{17}$$

The anisotropy parameter $b_E(v)$, however, has a very strong energy dependence, as can be seen also from Fig. 13, which for the considered values of v has the form

$$b_E(v=0)=6.296\exp(-1.723E^{0.44}),$$

$$b_E(v=11)=0.259\exp(-2.150E^{-0.95}). \tag{18}$$

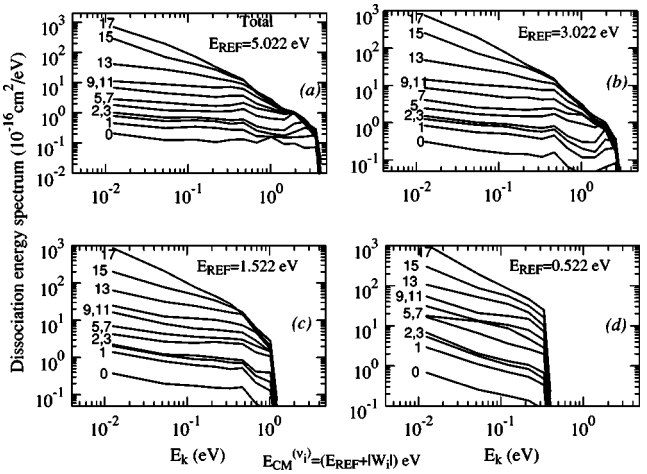

FIG. 12. The same as in Fig. 10, for $H+H_2^+(v_i)$ collisions.

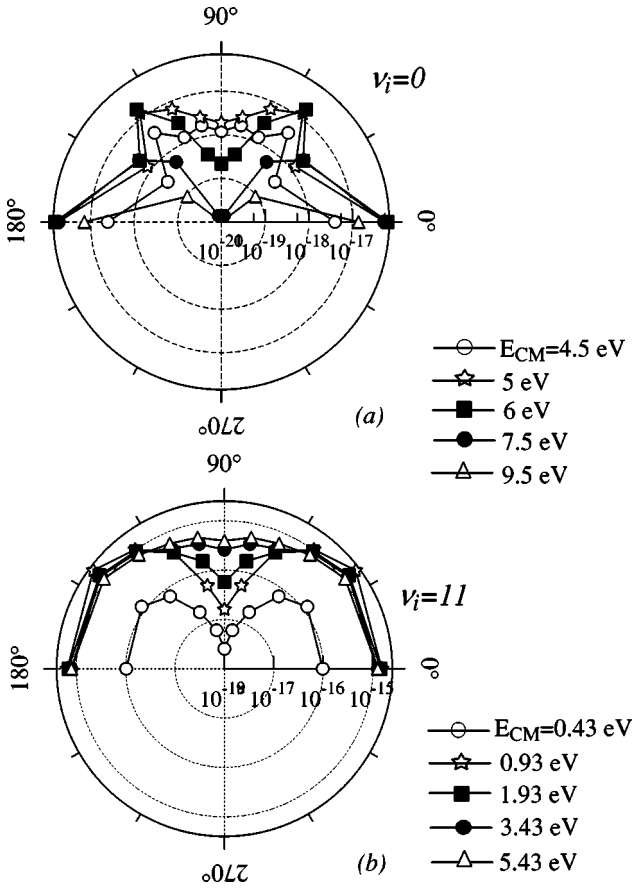

FIG. 13. Angular distributions of dissociation fragments in $H^+ + H_2(v_i)$ collisions, for various c.m. collision energies and $v_i = 0,11$.

The angular distributions of fragments from the $H+H_2^+$ dissociation have similar features as those shown in Fig. 13.

VI. SUMMARY

The dissociation processes of vibrationally excited $H_2(v_i)$ and of $H_2^+(v_i)$ in slow collisions with protons and hydrogen atoms, respectively, are studied in considerable detail. The principal dissociation mechanisms in the incoming stage of the collision are identified to be promotive series of Landau-Zener (avoided crossing) and S^*-type (hidden crossing) couplings at large and small values of reactive coordinate R, respectively. In the outgoing stage of the collision, the system can be promoted to the continuum by a (relatively weak) series of Q^*-type (hidden crossing) couplings, if the collision geometry is not far from the orthogonal. At small angles between the vector $\vec{R}$ of reactive coordinate and the orientation of molecular target axis, the Landau-Zener promotive series dominate the dissociation process at all values of reactive coordinate. Cross sections for the direct and charge-transfer dissociation channels for both $H^+ + H_2(v=0-14)$ and $H + H_2^+(v'=0-18)$ collision systems have been calculated in the center-of-mass collision energy range from the threshold to 9.5 eV. The calculation were performed by solving the Schrödinger equation for nuclear and electronic mo-

tion on the two lowest adiabatic electronic surfaces of H_3^+, by expanding the nuclear wave functions in a large vibrational basis of all discrete H_2 and H_2^+ states and corresponding discretized continua (altogether 900 states of positive and negative energy). The characteristic features of calculated DD and CTD dissociation cross sections are discussed, and the total cross sections are compared with those obtained by the classical TSH method [2]. The physical mechanism for various channels of dissociation are identified on the vibronic adiabatic diagrams, for various molecular target orientations. The energy and angular spectra of dissociated fragments are also calculated for various representative collision energies and initial vibrational states in both studied collision systems. The characteristic features of these spectra are also discussed.

ACKNOWLEDGMENT

We acknowledge support from the U.S. Department of Energy, Office of Fusion Energy Sciences, through Oak Ridge National Laboratory, managed by UT-Battelle, LLC under Contract No. DE-AC05-00OR22725.

[1] A. Yu. Pigarov and S. I. Krasheninnikov, Phys. Lett. A **222**, 251 (1996).
[2] A. Ichihara, O. Iwamoto, and R. K. Janev, J. Phys. B **33**, 4747 (2000).
[3] K. T. Tang, in *Theory of Chemical Reaction Dynamics II*, edited by M. Baer (CRC Press, Boca Raton, Fl, 1985).
[4] P. S. Krstić, Phys. Rev. A **66**, 042717 (2002).
[5] R. T. Pack, J. Chem. Phys. **60**, 633 (1974).
[6] D. Secrest, J. Chem. Phys. **62**, 710 (1975).
[7] M. Baer, G. Niedner, and J. P. Toennies, J. Chem. Phys. **88**, 1461 (1988).
[8] M. Baer, G. Niedner-Schatteburg, and J. P. Toennies, J. Chem. Phys. **91**, 4169 (1989).
[9] F. O. Ellison, J. Am. Chem. Soc. **85**, 3540 (1963).
[10] J. C. Tully and R. K. Preston, J. Chem. Phys. **55**, 562 (1971).
[11] M. J. Jamieson, A. Dalgarno, and J. N. Yukich, Phys. Rev. A **46**, 6956 (1992).
[12] P. S. Krstić and D. R. Schultz, J. Phys. B **32**, 2415 (1999).
[13] M. W. Schmidt, K. K. Baldridge, J. A. Boatz, S. T. Elbert, M. S. Gordon, J. H. Jensen, S. Koseki, N. Matsunaga, K. A. Nguyen, S. J. Su, T. L. Windus, M. Dupuis, and J. A. Montgomery, J. Comput. Chem. **14**, 1347 (1993).
[14] P. S. Krstić, D. R. Schultz, and R. K. Janev, Phys. Scr. **T96**, 61 (2002).
[15] M. Baer and H. Nakamura, J. Chem. Phys. **87**, 4651 (1987).
[16] L. M. Delves, Nucl. Phys. **20**, 275 (1960).
[17] Z. H. Top and M. Baer, J. Chem. Phys. **66**, 1363 (1977).
[18] *Theory of Chemical Reaction Dynamics*, edited by M. Baer (CRC Press, Boca Raton, Fl, 1985), Vol. I.
[19] E. A. Solov'ev, Usp. Fiz. Nauk **157**, 437 (1989) [Sov. Phys. Usp. **32**, 228 (1989)].
[20] P. S. Krstić, D. R. Schultz, and R. K. Janev, J. Phys. B **29**, 1941 (1996).
[21] J. C. Wells, I. Simbotin, and M. Gavrila, Phys. Rev. Lett. **80**, 3479 (1998).